

4D Radar-Inertial Odometry based on Gaussian Modeling and Multi-Hypothesis Scan Matching

Fernando Amodeo¹, Luis Merino, *Member, IEEE*¹ and Fernando Caballero¹

Abstract—4D millimeter-wave (mmWave) radars are sensors that provide robustness against adverse weather conditions (rain, snow, fog, etc.), and as such they are increasingly being used for odometry and SLAM applications. However, the noisy and sparse nature of the returned scan data proves to be a challenging obstacle for existing point cloud matching based solutions, especially those originally intended for more accurate sensors such as LiDAR. Inspired by visual odometry research around 3D Gaussian Splatting [8], in this paper we propose using freely positioned 3D Gaussians to create a summarized representation of a radar point cloud tolerant to sensor noise, and subsequently leverage its inherent probability distribution function for registration (similar to NDT [2]). Moreover, we propose simultaneously optimizing multiple scan matching hypotheses in order to further increase the robustness of the system against local optima of the function. Finally, we fuse our Gaussian modeling and scan matching algorithms into an EKF radar-inertial odometry system designed after current best practices. Experiments show that our Gaussian-based odometry is able to outperform current baselines on a well-known 4D radar dataset used for evaluation.

Our code and results can be publicly accessed at: <https://github.com/robotics-upo/gaussian-rio>

I. INTRODUCTION

4D millimeter-wave (mmWave) radars have earned considerable popularity in the world of robotics as an alternative to classic camera or LiDAR sensors due to their robustness against adverse weather conditions (rain, snow, fog, etc.), as well as their compact size and low power consumption. As such, there is considerable interest in incorporating these sensors in odometry and SLAM applications. Existing LiDAR odometry solutions have been applied, adapted and sometimes even further specialized to 4D radar, with varying degrees of success [24], [25], [26], [22], [20]. However, the point clouds generated by 4D radars are sparser, noisier, and have a narrower field of view compared to those generated by LiDARs; and as a result these algorithms often struggle with the geometry of certain scenes. Therefore, it is desirable to explore scene representations that directly model coarse-grained surfaces and regions of radar point clouds instead of focusing on individual points themselves.

Another technique that has gained popularity recently in the field of robotics is 3D Gaussian Splatting (3DGS) [8]. This algorithm creates an explicit representation of a visual scene, and has been applied to SLAM [12], [7], [1] as an alternative to existing methods using implicit representations such as NeRF [13]. However, 3DGS heavily relies on the nature of visual information for training and rendering, and

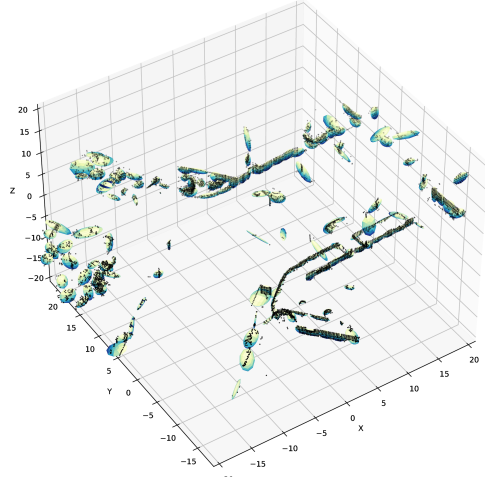


Fig. 1. Gaussian model of an example point cloud, containing 150 Gaussians. The surface of each spheroid represents the 2σ front of each Gaussian (i.e. Mahalanobis distance equal to two).

thus adapting it for use with LiDAR or radar instead of visual cameras is challenging; as opposed to NeRF, which can be straightforwardly adapted to model a SDF instead [14].

Inspired by both of these lines of research, in this paper we propose and describe methods for obtaining a Gaussian model representation of a point cloud, and performing registration of a point cloud with respect to an existing Gaussian model. While this is similar in principle to the Normal Distributions Transform (NDT) [2], our methods consider Gaussians to be arbitrarily positioned in space instead of following a regular grid – like 3DGS [8]. Moreover, our scan matching (registration) step considers multiple simultaneous hypotheses, which can help increase the performance of the system, as we show in our experiments.

Figure 2 shows the overall pipeline of our odometry system. As in other solutions, we use an Extended Kalman Filter (EKF) to perform inertial strapdown and process sensory input, including radar egoveloccity. Keyframing is used to select individual 4D radar scans, which then undergo Gaussian modeling. The Gaussian multi-hypothesis scan matching algorithm registers every incoming 4D radar scan against the Gaussian model in order to produce a relative pose observation with respect to the last keyframe, which is then used to further update the EKF. Our experiments show how these Gaussian-based modeling and registration processes improve the results of existing state-of-the-art 4D radar-inertial odometry baselines.

¹Service Robotics Laboratory – Universidad Pablo de Olavide (Seville), Spain {famozur, lmercab, fcaballero}@upo.es

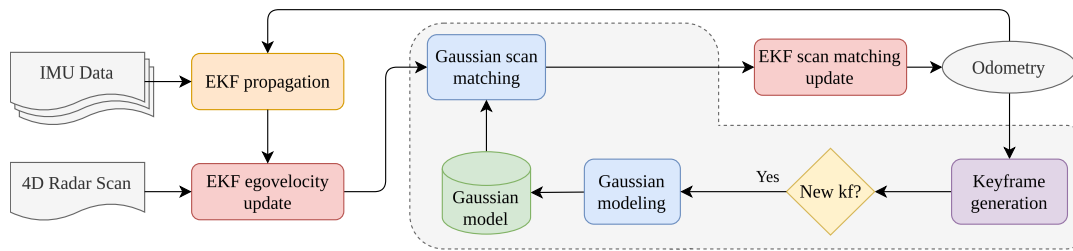


Fig. 2. Overview of the proposed Gaussian radar-inertial odometry pipeline

This paper is organized as follows: Section II reviews existing related literature, Sections III, IV and V describe the three main components of our method respectively: Gaussian modeling, Gaussian scan matching, and the Extended Kalman Filter tying everything together; Section VI shows experimental results, and Section VII closes the paper with some conclusions.

II. RELATED WORK

A. Inertial odometry and SLAM

There exist a large number of works focused on Inertial Odometry, sometimes even attaining a full SLAM pipeline (including loop closure). Particularly we are interested in approaches that use non-visual sensors, such as [23], [21], [15], [3], [4], [24], [25], [26], [22], [20]. These works use a 3D LiDAR (LIO) or 4D radar (RIO) sensor together with an IMU to provide an odometry solution. The main technical advantage of these sensors over visual sensors (cameras) is their increased field/depth of view and robustness to adverse environmental conditions: in particular, both are immune to low light conditions, and 4D radar in addition offers robustness to fog, dust and rain. Moreover, 4D radar is uniquely capable of measuring the velocity of objects by leveraging the Doppler effect. Researchers have taken advantage of this to directly measure the robot’s own velocity (“egovelocity”) [3], [4], something which has been shown to significantly improve the performance of odometry systems.

Registration of incoming point clouds with respect to previous ones is a key technique used in odometry systems. In particular, the most widely used algorithm for aligning point clouds is Generalized Iterative Closest Point (GICP) [17]. In the case of radar scans, this is a more difficult task compared to LiDAR because of the lower number and density of points, as well as higher measurement noise/uncertainty in each point’s position. For this reason [26] proposed the Adaptive Probability Distribution variant of the algorithm (APDGICP), which leverages GICP’s ability to make use of the spatial probability distribution of each point, calculating the required point position covariance matrices according to the radar specifications. However, this is still in essence an approach focused on individual points, without attempting to extract larger scale geometric features that may be more stable and robust for registration purposes.

B. Gaussian-based modeling

The Normal Distributions Transform (NDT) algorithm [2] slices and subdivides a point cloud using a regular grid and computes normal distributions for each cell that contains points. Scan matching is performed by maximizing the resulting probability distribution function with respect to an incoming scan. An important limitation of this algorithm is the fact that the grid structure itself imposes restrictions on the geometry, and the resulting model may not be fine grained enough to accurately model the geometry of the environment. Another problem lies in the fact that discontinuities in the probability function are produced when partially registered points cross cell boundaries during optimization. Moreover, the original authors only consider 2D scan matching (requiring 3D point clouds to be projected into the XY plane), although subsequent works [11] extend the algorithm to 3D. NDT has been used with radar scans too [10], although only for pure radar odometry as opposed to radar-inertial odometry, and without leveraging radar egovelocity information.

3D Gaussian Splatting (3DGS) [8] is a popular technique for creating a model of a scene from multiple posed images. A 3DGS model is a collection of multiple 3D normal distributions (Gaussians) freely distributed in space, each also containing color/radiance information encoded using spherical harmonics. Even though this technique was originally developed as an alternative to NeRF [13] for novel view synthesis, researchers have successfully leveraged this representation to develop SLAM solutions [12], [7], [1]. However, 3DGS and these works are all designed for visual sensors (cameras), and they cannot leverage other sensors such as LiDAR or radar due to the nature of the representation. This affects the rendering process in particular: while NeRF’s ray casting framework can be easily adapted to directly predict the output of a SDF [14] (therefore removing the volume rendering component from the system), the differentiable tile rasterizer is a core part of 3DGS that cannot be avoided, neither during training nor inference.

III. GAUSSIAN MODELING

Given a point cloud \mathcal{P} containing M points $\{\mathbf{p}_i | i = 0, 1, \dots, M\}$ with $\mathbf{p}_i \in \mathbb{R}^3$, our goal is creating a summarized representation of its geometry for use with downstream tasks such as mapping or localization. Following the line of works such as NDT [2] and 3DGS [8], we decided to model the geometry using normal distributions. Figure 1 shows an example of a Gaussian model.

A. Parametrization

We parametrize the Gaussian model \mathcal{G} of a scene as a collection of N independent trivariate normal distributions (**3D Gaussians**), each modeling the geometry of an individual region in space. The model is described by the following parameters of each Gaussian $\theta_j = \{\boldsymbol{\mu}_j, \mathbf{s}_j, \mathbf{q}_j\}$:

- Center point $\boldsymbol{\mu}_j \in \mathbb{R}^3$, indicating the mean of the distribution.
- Scaling vector $\mathbf{s}_j \in \mathbb{R}^3$, indicating the natural logarithms of the square roots of the eigenvalues of the covariance matrix.
- Rotation quaternion $\mathbf{q}_j \in \mathbb{H}$, compactly encoding the eigenvectors of the covariance matrix (see below); where \mathbb{H} is the field of quaternions.

Unlike in Gaussian Mixture Models (GMMs), we do not define π_j weight parameters for the prior probability of a point being generated by a given Gaussian. This is because point cloud data does not encode a complete population of points – it merely represents a *sample* of said population, biased by factors such as the physical geometric properties of the sensor. For instance, sampling density is inversely proportional to distance from the sensor. This means we cannot model these prior probabilities, and as such we only consider posterior probabilities after a point is assigned to a Gaussian (through other non-probabilistic means, such as measuring distances).

The scaling and rotation parameters succinctly describe the covariance matrix of a normal distribution [19], [5]. To see why this is possible, we first derive a rotation matrix $\mathbf{R}_j = \mathbf{R}\{\mathbf{q}_j\}$, and a scaling matrix $\mathbf{S}_j = \text{diag}(\exp_{\circ}(\mathbf{s}_j))$, where $\exp_{\circ}(\mathbf{x})$ is element-wise natural exponentiation and $\mathbf{R}\{\mathbf{q}\}$ is the quaternion-to-rotation-matrix conversion operator. We then define a transformation matrix $\mathbf{M}_j = \mathbf{R}_j \mathbf{S}_j$ that maps a mean-centered point into the Gaussian’s correlation space, and finally derive the covariance matrix $\boldsymbol{\Sigma}_j = \mathbf{M}_j \mathbf{M}_j^T$ of the distribution.

In addition, the auxiliary parameters \hat{s}_j and $\hat{\mathbf{q}}_j$ are defined and used during optimization, such that $\hat{s}_j = \max_{\circ}(s_{\min}, \mathbf{s}_j)$ and $\hat{\mathbf{q}}_j = \frac{\mathbf{q}_j}{|\hat{\mathbf{q}}_j|}$ (\max_{\circ} being the element-wise max operator). This transformation allows us to define a minimum log scale factor s_{\min} to prevent Gaussians from becoming infinitely small (and Mahalanobis distances infinitely big); and also enforce that $\hat{\mathbf{q}}_j$ must be a unit quaternion. Typically we make the minimum size equal to the radar point uncertainty (standard deviation of position noise).

B. Initialization

The model \mathcal{G} is initialized with all \mathbf{s}_j set to 0 (indicating unit scale), and all $\hat{\mathbf{q}}_j$ set to the unit quaternion. As for $\boldsymbol{\mu}_j$, we perform a Bisecting K-Means clustering to find initial estimates for the centers of the Gaussians.

C. Optimization

\mathcal{G} is optimized iteratively using gradient descent. Each epoch involves the following steps:

- Each point of \mathcal{P} is matched to the nearest Gaussian center point $\boldsymbol{\mu}_j$. This process builds a set G_j for each

Gaussian, containing all matched points. We use the standard Euclidean distance in this step as opposed to the Mahalanobis distance in order to avoid a feedback loop between center and covariance matrix optimization that results in exploding gradients.

- Each point \mathbf{p}_i is transformed to the coordinate space of its assigned Gaussian as such: $\hat{\mathbf{p}}_i = \mathbf{M}_j^{-1}(\mathbf{p}_i - \boldsymbol{\mu}_j)$. Note that $\mathbf{M}_j^{-1} = \mathbf{S}_j^{-1} \mathbf{R}_j^T$, and \mathbf{S}_j^{-1} is trivial to calculate since \mathbf{S}_j is a diagonal matrix.
- The parameters of \mathcal{G} (in other words, all θ_j) are updated using the gradient of the loss function.

We define the following loss function affecting a given θ_j :

$$\mathcal{L}_j = \frac{1}{2|G_j|} \sum_{\mathbf{p}_i \in G_j} \hat{\mathbf{p}}_i^T \hat{\mathbf{p}}_i + \sum_k \hat{s}_{jk} + \left(\min_k \hat{s}_{jk} - s_{\text{disc}} \right)^+, \quad (1)$$

where $x^+ = \max(0, x)$, and s_{disc} is a hyperparameter that introduces a log size prior for the smallest dimension of the Gaussian, encouraging it to be shaped like a thin disc (better suited to modeling surfaces).

To see how the other terms of the loss function are derived, first we introduce the log PDF of the multivariate normal distribution, which we need to maximize, so we flip its sign:

$$-\log P(\mathbf{p}_i | \theta_j) = K + \frac{1}{2} \log |\boldsymbol{\Sigma}_j| + \frac{1}{2} (\mathbf{p}_i - \boldsymbol{\mu}_j)^T \boldsymbol{\Sigma}_j^{-1} (\mathbf{p}_i - \boldsymbol{\mu}_j). \quad (2)$$

Note that K is a constant correction factor that enforces $\int_{-\infty}^{\infty} P(x) dx = 1$, and we can ignore it for the purposes of optimization. The term involving the determinant $|\boldsymbol{\Sigma}_j|$ can be simplified using our parametrization:

$$|\boldsymbol{\Sigma}_j| = |\mathbf{M}_j| |\mathbf{M}_j^T| = |\mathbf{R}_j| |\mathbf{S}_j|^2 |\mathbf{R}_j^T| = |\mathbf{S}_j|^2 = \left(\prod_k e^{\hat{s}_{jk}} \right)^2, \quad (3)$$

and thus,

$$\frac{1}{2} \log |\boldsymbol{\Sigma}_j| = \frac{1}{2} 2 \sum_k \log e^{\hat{s}_{jk}} = \sum_k \hat{s}_{jk}. \quad (4)$$

Likewise, we can simplify the term involving p_i . Note that it is half of the square of the Mahalanobis distance between the point and the Gaussian. The matrix $\boldsymbol{\Sigma}_j^{-1}$ can be decomposed as such: $\boldsymbol{\Sigma}_j^{-1} = (\mathbf{M}_j^T)^{-1} \mathbf{M}_j^{-1} = (\mathbf{M}_j^{-1})^T \mathbf{M}_j^{-1}$. We can substitute it in the term and simplify:

$$\frac{1}{2} (\mathbf{p}_i - \boldsymbol{\mu}_j)^T \boldsymbol{\Sigma}_j^{-1} (\mathbf{p}_i - \boldsymbol{\mu}_j) = \frac{1}{2} (\mathbf{p}_i - \boldsymbol{\mu}_j)^T (\mathbf{M}_j^{-1})^T \cdot \mathbf{M}_j^{-1} (\mathbf{p}_i - \boldsymbol{\mu}_j) = \frac{1}{2} \hat{\mathbf{p}}_i^T \hat{\mathbf{p}}_i. \quad (5)$$

Lastly, we convert the (per-point) log probability function into a per-Gaussian loss function by taking the mean log probability value across all points assigned to the Gaussian.

This has the effect of introducing the $\frac{1}{|G_j|}$ factor in the Mahalanobis term, and has no effect in the determinant term since it is constant for all points within the Gaussian. We decided to aggregate with the mean in order to ensure that every Gaussian equally contributes towards the loss function, instead of being biased towards Gaussians with larger G_j sets. The resulting loss function \mathcal{L} of the entire model \mathcal{G} can be finally obtained by once again taking the mean of the loss values across all Gaussians.

IV. GAUSSIAN MULTI-HYPOTHESIS SCAN MATCHING

Given a Gaussian model \mathcal{G} and a point cloud \mathcal{P} , we define a registration process that estimates the pose of the robot ξ with respect to \mathcal{G} . The algorithm is based on the simultaneous optimization of multiple hypotheses centered around the current predicted position of the robot, in order to increase the robustness against local optima.

A. Definitions

We define the robot pose ξ to be a member of $SE(3)$; that is, it includes a translational component $\mathbf{t} \in \mathbb{R}^3$ and rotational component $\mathbf{q} \in SO(3)$, with respect to *some* frame of reference. We consider that the uncertainty about the true robot pose follows *some* probability distribution: $\xi \sim P$. Given a suitable model of P , we can randomly sample a swarm of K pose particles $\hat{\xi}^k$, each representing a different hypothesis, and use an optimization algorithm that evaluates each particle against \mathcal{G} to further refine these estimates until one of the particles reaches a suitable optimum. We believe exploring the solution space using a particle swarm increases robustness in challenging situations, especially when dealing with large rotations or translations.

B. Optimization

The process is performed iteratively using gradient descent. Each epoch involves the following steps:

- We define K virtual copies of \mathcal{P} called $\mathcal{P}^{/k}$, each registered according to every pose hypothesis $\hat{\xi}^k$. We also suggest downsampling the point cloud before creating the copies in order to reduce the computational load while retaining a representative sample of the geometry captured by the point cloud.
- Every point \mathbf{p}_i^k of $\mathcal{P}^{/k}$ is matched to the Gaussian θ_j in \mathcal{G} that results in the lowest Mahalanobis distance, which we call d_i^k .
- We calculate the loss function and perform gradient descent on $\hat{\xi}^k$.

The loss function used is simply

$$\mathcal{L}_k = \frac{1}{M} \sum_i^M \min(d_i^k, d_{\max}); \quad \mathcal{L} = \sum_i^K \mathcal{L}_i, \quad (6)$$

where d_{\max} is the maximum Mahalanobis distance allowed, \mathcal{L}_k is the loss function associated to a given particle $\hat{\xi}^k$, and \mathcal{L} is the loss function affecting the entire swarm. Once the optimization process stops, we can select the particle with the lowest loss as the resulting output pose of the registration algorithm.

C. Keyframing

A common technique used in odometry systems is keyframing. Certain poses of the robot are selected to become local reference points (keyframes) that are later used for registration, graph optimization or loop closure purposes. In our case, we use keyframing to select individual radar point clouds to undergo Gaussian modeling, and serve as reference for Gaussian scan matching of subsequent radar point clouds. This has the benefit of reducing the accumulated error that arises from successive applications of the scan matching algorithm, though it also means the criteria used to select keyframe candidates needs to be carefully designed to generate the appropriate keyframe pacing. We use a simple set of criteria to decide when a new pose ξ^j qualifies to become a new keyframe. Given the most recent keyframe ξ^i , we can derive the $SE(3)$ transformation relative to the keyframe $T = \xi^j \ominus \xi^i = \{\mathbf{t}, \mathbf{q}\}$. The criteria are then simply that any of the following must hold:

- For the translational component: $\|\mathbf{t}\|_2 \geq d_{\max}$, where d_{\max} is the maximum distance threshold.
- For the rotational component: $2 \cos^{-1} |q_w| \geq \alpha_{\max}$, where α_{\max} is the maximum rotation angle threshold.

V. INERTIAL ODOMETRY WITH EKF

We use an Extended Kalman Filter in our odometry solution to tightly integrate all incoming sensor information: inertial data, radar egoveLOCITY observations, and scan matching results. Unlike other published solutions [18], [3], [4], we only use Error State filtering for the attitude, as opposed to the entire state. The state (\mathbf{x}), control (\mathbf{u}) and noise (\mathbf{w}) vectors of the filter are the following:

$$\mathbf{x} = \begin{bmatrix} \mathbf{p} \\ \mathbf{v} \\ \mathbf{b}_a \\ \mathbf{b}_\omega \\ \delta\boldsymbol{\theta} \end{bmatrix}; \quad \mathbf{u} = \begin{bmatrix} \mathbf{a} \\ \boldsymbol{\omega} \end{bmatrix}; \quad \mathbf{w} = \begin{bmatrix} \mathbf{w}_v \\ \mathbf{w}_\theta \\ \mathbf{w}_a \\ \mathbf{w}_\omega \\ \mathbf{w}_{b_a} \\ \mathbf{w}_{b_\omega} \end{bmatrix}, \quad (7)$$

where \mathbf{p} is the position, \mathbf{v} is the velocity, \mathbf{b}_a and \mathbf{b}_ω are the accelerometer/gyroscope biases, $\delta\boldsymbol{\theta}$ is the attitude error expressed as a tangential rotation $\in \mathfrak{so}(3)$, and \mathbf{a} and $\boldsymbol{\omega}$ are the IMU accelerometer/gyroscope readings. Velocity and attitude process noise are modeled by \mathbf{w}_v and \mathbf{w}_θ respectively. Note that the attitude quaternion \mathbf{q} is not included in \mathbf{x} , and the attitude error $\delta\boldsymbol{\theta}$ (which takes its place in \mathbf{x}) is nominally always 0. We follow Kalibr's IMU noise model [16]¹, and consider both additive ($\mathbf{w}_a, \mathbf{w}_\omega$) and random walk noise ($\mathbf{w}_{b_a}, \mathbf{w}_{b_\omega}$) in accelerometer/gyroscope readings.

We employ the right-handed North-West-Up (NWU) convention typical of robotics, and consider three reference frames: world (w), body/IMU (b) and radar (r). The rotation matrix \mathbf{C}_f^g transforms a vector from frame f to frame g , likewise $\mathbf{C}_g^f = (\mathbf{C}_f^g)^T$. We define $\mathbf{C}_b^w = \mathbf{R}\{\delta\mathbf{q}\}\mathbf{R}\{\mathbf{q}\}$, approximating $\mathbf{R}\{\delta\mathbf{q}\} = \exp([\delta\boldsymbol{\theta}]_\times) \approx \mathbf{I} + [\delta\boldsymbol{\theta}]_\times$ for the purposes of linearization, and \mathbf{C}_r^b is given as a parameter.

¹<https://github.com/ethz-asl/kalibr/wiki/IMU-Noise-Model>

All state parameters (\mathbf{p} , \mathbf{v} , \mathbf{q}) are expressed in the world frame.

There also exists a vector $\mathbf{g} = -[0 \ 0 \ 9.80511]^T$ modeling the Earth's gravity. We consider it a constant outside the scope of the EKF, which also has the intended effect of synchronizing the roll/pitch components of the attitude to be relative to the plane tangent to the Earth's surface. We do not consider long enough travel distances for changes in the tangent plane to matter.

A. EKF initialization

We initialize the state vector \mathbf{x} to 0, attitude \mathbf{q} to the unit quaternion, and covariance matrix \mathbf{P} to 0 except for the following sub-blocks:

$$\mathbf{P}_{b_a b_a} = \mathbf{I}\eta_{b_a}^2; \mathbf{P}_{b_\omega b_\omega} = \mathbf{I}\eta_{b_\omega}^2; \mathbf{P}_{\delta\theta_{xy} \delta\theta_{xy}} = \mathbf{I}\eta_\theta^2, \quad (8)$$

where η_{b_a} , η_{b_ω} and η_θ are the initial uncertainties (standard deviations) of the accelerometer bias, gyroscope bias and roll/pitch attitude error. We consider the initial yaw attitude uncertainty to be zero because we are not incorporating a compass/magnetometer.

B. EKF propagation

We use a simplified inertial strapdown formulation that assumes movement to be linear instead of being perturbed by the current angular velocity reading of the gyroscope, due to the short time interval and small change in attitude (in effect equivalent to first order integration):

$$\mathbf{p} \leftarrow \mathbf{p} + \mathbf{v}t + \frac{1}{2}(\mathbf{C}_b^w(\mathbf{a} - \mathbf{b}_a) + \mathbf{g})t^2, \quad (9)$$

$$\mathbf{v} \leftarrow \mathbf{v} + (\mathbf{C}_b^w(\mathbf{a} - \mathbf{b}_a) + \mathbf{g})t, \quad (10)$$

$$\mathbf{q} \leftarrow \mathbf{q} \otimes \exp\left(\frac{1}{2}(\boldsymbol{\omega} - \mathbf{b}_\omega)t\right). \quad (11)$$

The strapdown formulation is linearized in order to propagate the covariance matrix:

$$\mathbf{P} \leftarrow \mathbf{F}\mathbf{P}\mathbf{F}^T + \mathbf{N}\mathbf{Q}\mathbf{N}^T, \quad (12)$$

where \mathbf{F} is the linearized state transition matrix, \mathbf{Q} is the noise covariance matrix, and \mathbf{N} is the noise state transition matrix. These three matrices are sparsely populated: $\mathbf{F} = \mathbf{I}$ and $\mathbf{Q} = \mathbf{N} = \mathbf{0}$, except for the following subblocks:

$$\mathbf{F}_{pv} = \mathbf{I}t; \mathbf{F}_{pb_a} = -\frac{1}{2}\mathbf{C}_b^w t^2; \mathbf{F}_{p\delta\theta} = -\frac{1}{2}[\mathbf{C}_b^w \mathbf{a}]_\times t^2; \quad (13)$$

$$\mathbf{F}_{vb_a} = \mathbf{F}_{\delta\theta b_\omega} = -\mathbf{C}_b^w t; \mathbf{F}_{v\delta\theta} = -[\mathbf{C}_b^w \mathbf{a}]_\times t; \quad (14)$$

$$\mathbf{Q}_{vv} = \mathbf{I}\sigma_v^2; \mathbf{Q}_{\theta\theta} = \mathbf{I}\sigma_\theta^2; \mathbf{Q}_{a_a} = \mathbf{I}\frac{\sigma_a^2}{t}; \quad (15)$$

$$\mathbf{Q}_{\omega\omega} = \mathbf{I}\frac{\sigma_\omega^2}{t}; \mathbf{Q}_{b_a b_a} = \mathbf{I}\sigma_{b_a}^2 t; \mathbf{Q}_{b_\omega b_\omega} = \mathbf{I}\sigma_{b_\omega}^2 t; \quad (16)$$

$$\mathbf{N}_{pa} = \frac{1}{2}\mathbf{C}_b^w t^2; \mathbf{N}_{va} = \mathbf{N}_{\delta\theta\omega} = \mathbf{C}_b^w t; \quad (17)$$

$$\mathbf{N}_{vv} = \mathbf{N}_{\delta\theta\theta} = \mathbf{N}_{b_a b_a} = \mathbf{N}_{b_\omega b_\omega} = \mathbf{I}, \quad (18)$$

where σ_v , σ_θ , σ_a , σ_ω , σ_{b_a} and σ_{b_ω} are the standard deviations of the respective components of \mathbf{w} .

C. EKF update and error state reset

Given observation \mathbf{y} , residual observation vector \mathbf{r} , observation covariance matrix \mathbf{R} and linearized observation matrix \mathbf{H} (so that $\mathbf{r} \approx \mathbf{y} - \mathbf{H}\mathbf{x}$), we can proceed to apply the Kalman filter equations (in Joseph form):

$$\mathbf{K} = \mathbf{P}\mathbf{H}^T(\mathbf{H}\mathbf{P}\mathbf{H}^T + \mathbf{R})^{-1}; \mathbf{L} = \mathbf{I} - \mathbf{K}\mathbf{H}, \quad (19)$$

$$\mathbf{x} \leftarrow \mathbf{x} + \mathbf{K}\mathbf{r}; \mathbf{P} \leftarrow \mathbf{L}\mathbf{P}\mathbf{L}^T + \mathbf{K}\mathbf{R}\mathbf{K}^T. \quad (20)$$

As previously mentioned, the attitude part of the robot's pose is expressed as error state in the EKF, and after an EKF update the nominal value of $\delta\boldsymbol{\theta}$ becomes non-zero, making it necessary to incorporate the estimated error back into the state as follows:

$$\mathbf{q} \leftarrow \delta\mathbf{q} \otimes \mathbf{q}; \delta\mathbf{q} = \exp\left(\frac{1}{2}\delta\boldsymbol{\theta}\right), \quad (21)$$

$$\delta\boldsymbol{\theta} \leftarrow \mathbf{0}; \mathbf{P} \leftarrow \mathbf{G}\mathbf{P}\mathbf{G}^T; \mathbf{G}_{\delta\theta\delta\theta} = \mathbf{R}\{\delta\mathbf{q}\}, \quad (22)$$

where \mathbf{G} is the error reset matrix, and it is a sparse matrix equal to \mathbf{I} except for the given subblock.

D. Radar egoveloccity observation

Following previous works, we directly observe the robot's velocity by leveraging the Doppler effect in measurements returned by the radar. The returned point cloud is first transformed by \mathbf{C}_r^b to match the IMU orientation (we consider the separation between IMU and radar to be negligible). Afterwards, we use the RANSAC-LSQ algorithm [3] to both filter out outlier (dynamic) points, and estimate the current body-frame velocity of the robot, including a covariance matrix. The filtered point cloud is also fed to the Gaussian modeling and scan matching algorithm in the following subsection. The observation model used to perform the EKF update is as follows:

$$\mathbf{r} = \mathbf{y} - \mathbf{C}_w^b \mathbf{v}; \mathbf{H}_{:v} = \mathbf{C}_w^b; \mathbf{H}_{:\delta\theta} = \mathbf{C}_w^b[\mathbf{v}]_\times. \quad (23)$$

E. Scan matching observation

The Gaussian modeling and scan matching algorithms allow us to observe robot poses relative to previous keyframes. In other words, given a keyframe pose ξ^k we can observe the change in translation and rotation that has occurred since said keyframe. We initialize the pose particle swarm with a distribution $\mathbf{P} \sim \mathcal{N}(\xi^x, \boldsymbol{\Sigma})$ where ξ^x is the relative robot pose formed from the current nominal state of the EKF: $\xi^x = \{\mathbf{p}, \mathbf{q}\} \ominus \xi^k$, and $\boldsymbol{\Sigma}$ is a covariance matrix indicating the desired dispersion of the particles for each of the 6 degrees of freedom (X/Y/Z/roll/pitch/yaw). Afterwards, we apply the scan matching algorithm and obtain an optimized observation pose ξ^y , from which a residual pose can be obtained: $\xi^r = \xi^y \ominus \xi^x = \{\delta\mathbf{p}, \delta\mathbf{q}\}$. Since the attitude error quaternion $\delta\mathbf{q}$ can be approximated as $\delta\mathbf{q} = \exp\left(\frac{1}{2}\delta\boldsymbol{\theta}\right) \approx [1 \ \frac{1}{2}\delta\boldsymbol{\theta}^T]^T$ for very small errors, the attitude error vector can be approximated as $\delta\boldsymbol{\theta} \approx \frac{2}{\delta q_w} \delta\mathbf{q}_v$. This allows us to construct the residual vector $\mathbf{r} = [\delta\mathbf{p}^T \ \delta\boldsymbol{\theta}^T]^T$ to be fed to

the EKF update equation – note that this vector contains X/Y/Z/roll/pitch/yaw components (in this order). The non-zero subblocks of the observation matrix \mathbf{H} can be defined as such: $\mathbf{H}_{\delta p p} = \mathbf{H}_{\delta \theta \delta \theta} = \mathbf{C}_w^k$, where k corresponds to the keyframe’s reference frame. We are currently using a fixed observation covariance matrix \mathbf{R} , although we believe it should be possible to leverage the optimized particle swarm returned by the scan matching algorithm to estimate this matrix.

Furthermore, we constrain the observation model described above by removing degrees of freedom that are deemed noisy in the scan matching due to the properties of the sensor. For example, radars have lower resolution in the Z axis, which degrades the usefulness of Z/roll/pitch information returned by scan matching algorithms. In order to ignore the unreliable degrees of freedom, we transform the residual vector $\mathbf{H}_c \mathbf{r}$, observation matrix $\mathbf{H}_c \mathbf{H}$ and covariance matrix $\mathbf{H}_c \mathbf{R} \mathbf{H}_c^T$ by a constraint matrix defined as follows:

$$\mathbf{H}_c = \begin{bmatrix} 1 & 0 & 0 & 0 & 0 & 0 \\ 0 & 1 & 0 & 0 & 0 & 0 \\ 0 & 0 & 0 & 0 & 0 & 1 \end{bmatrix}. \quad (24)$$

VI. EXPERIMENTAL RESULTS

We compare our odometry with previous published 4D radar-inertial odometry methods on the NTU4DRadLM dataset [25]. These include the GICP and Fast-LIO baselines tested in the original NTU4DRadLM paper, the APDGICP algorithm tested in the follow-up 4DRadarSLAM paper [26], as well as other works such as EFEAR-4D [22] or RIV-SLAM [20]. We compare versions of these methods without loop closure if possible, in order to focus on evaluating pure odometry. Out of the six sequences present in NTU4DRadLM, we perform evaluation using four: cp and ny1 (low speed regime, using a handcart platform), and loop2 and loop3 (high speed regime, using a car platform). The garden and loop1 sequences cannot be reliably used for evaluation because they contain large gaps in the IMU and radar data, respectively.

We evaluate relative translation/rotation errors using the modern and flexible *evo* evaluation package [6], as well as the older *rpg_trajectory_evaluation* package [27] used by previous works, using default settings. In the case of *evo* we use a custom evaluation script written specifically to follow the default behavior of *rpg_trajectory_evaluation* as closely as possible. We run both evaluation packages on the baseline GICP and Fast-LIO trajectories published along with the NTU4DRadLM dataset, as well as the trajectories generated by our odometry solution. In particular, we report results for the full version of our method, and also two ablated versions: one that replaces the Gaussian modeling and scan matching with GICP, and another that uses single-hypothesis scan matching. The GICP version uses *small_gicp* [9] as the underlying implementation, and in both ablations we use the current nominal state of the EKF directly as the initial estimate (instead of sampling a random particle swarm). We also include the self-reported metrics

for all methods that appear in their respective papers as-is, since the trajectory files needed for metric calculation are not available.

The source code of our odometry solution can be accessed online on GitHub². We include the script used to generate the odometry trajectories, and the script used to evaluate trajectories with *evo*. The code also contains all details regarding the system parameters we used, such as EKF covariance initialization, IMU/noise parameters, number of Gaussians, etc.

A. Quantitative Analysis

1) *Evaluation with evo*: In Table I, we can observe major improvements in all 4 sequences provided by our method compared to the baselines originally tested by the authors of NTU4DRadLM. Moreover, the comparison between the Gaussian versions of our method and our GICP ablation shows improvements in relative translation error (t_{rel}) in 3 out of 4 sequences, and improvements in relative rotation error (r_{rel}) in 3 out of 4 sequences. In particular, the best improvements can be seen in the ny1 sequence. The version with scan matching based on multiple hypotheses overperforms the version with a single hypothesis in 3 out of 4 sequences. We theorize that the sequences where our GICP ablation overperforms Gaussian versions of our method contain more challenging/sparser geometry due to being higher speed car driving sequences in open environments. Nonetheless, we believe it should be possible to further adjust the hyperparameters used (such as number of Gaussians used for modeling, number of hypotheses used for scan matching, keyframe thresholds, EKF covariances used, etc.) in order to optimize the algorithm for those sequences.

2) *Evaluation with rpg_trajectory_evaluation*: In Table II, we note discrepancies in the NTU4DRadLM baseline metrics between the reported values in the paper and the values obtained by running the evaluation software on the corresponding published trajectories, especially in the higher speed sequences. We also note very similar results for all methods generated by both evaluation packages, validating the use of both packages for evaluating 4D radar-inertial odometry methods. The errors reported by EFEAR-4D for the higher speed sequences are much higher than the values reported by other methods. We believe this to be caused by some difference in the evaluation methodology, as the same paper reports similar errors for baseline methods such as [26]. The most challenging sequence is loop3, and interestingly the best results are the ones reported by the NTU4DRadLM authors for the simplest baseline method. RIV-SLAM is the best performing method in loop2, however it must be said that to the best of our knowledge this method includes loop closure. The second best performing method in that sequence is the single-hypothesis version of our method, in line with the results in Table I.

²<https://github.com/robotics-upo/gaussian-rio>

TABLE I
 QUANTITATIVE ANALYSIS ON NTU4DRadLM DATASET USING EVO. BEST RESULTS IN BOLD, SECOND BEST RESULTS UNDERLINED

| | cp | | nyl | | loop2 | | loop3 | |
|------------------------------------|---------------|-----------------|---------------|-----------------|---------------|-----------------|---------------|-----------------|
| | t_{rel} (%) | r_{rel} (°/m) | t_{rel} (%) | r_{rel} (°/m) | t_{rel} (%) | r_{rel} (°/m) | t_{rel} (%) | r_{rel} (°/m) |
| NTU4DRadLM baseline: gicp [25] | 4.87 | 0.0648 | 5.65 | 0.0257 | 6.73 | 0.0094 | 6.03 | 0.0097 |
| NTU4DRadLM baseline: Fast-LIO [25] | 3.97 | 0.0773 | 4.47 | 0.0273 | 8.38 | 0.0096 | 6.95 | 0.0105 |
| Our method (GICP scan matching) | 1.69 | 0.0323 | 4.50 | 0.0198 | 3.92 | <u>0.0044</u> | 3.81 | 0.0054 |
| Our method (single hypothesis) | <u>1.47</u> | 0.0284 | <u>3.17</u> | 0.0150 | 2.95 | 0.0043 | 4.80 | 0.0065 |
| Our method (full version) | 1.33 | 0.0260 | 2.92 | 0.0134 | <u>3.49</u> | 0.0047 | <u>4.55</u> | <u>0.0061</u> |

TABLE II
 QUANTITATIVE ANALYSIS ON NTU4DRadLM DATASET USING RPG_TRAJECTORY_EVALUATION. METHODS MARKED WITH * ARE SELF-REPORTED METRICS

| | cp | | nyl | | loop2 | | loop3 | |
|-------------------------------------|---------------|-----------------|---------------|-----------------|---------------|-----------------|---------------|-----------------|
| | t_{rel} (%) | r_{rel} (°/m) | t_{rel} (%) | r_{rel} (°/m) | t_{rel} (%) | r_{rel} (°/m) | t_{rel} (%) | r_{rel} (°/m) |
| NTU4DRadLM baseline: gicp* [25] | 4.13 | 0.0552 | 4.62 | 0.0184 | 4.84 | 0.0060 | 3.22 | 0.0060 |
| NTU4DRadLM baseline: Fast-LIO* [25] | 2.94 | 0.0468 | 3.80 | 0.0208 | 7.16 | 0.0057 | 4.55 | 0.0064 |
| 4DRadarSLAM apdgicp* [26] | 3.56 | 0.0369 | 3.55 | 0.0171 | 6.09 | 0.0082 | 4.09 | 0.0097 |
| EFEAR-4D* [22] | 5.09 | 0.0125 | 8.93 | 0.0166 | 37.27 | 0.0152 | 37.01 | 0.0175 |
| RIV-SLAM* [20] | 2.58 | 0.0342 | — | — | 2.69 | 0.0456 | — | — |
| NTU4DRadLM baseline: gicp [25] | 4.921 | 0.068 | 5.775 | 0.027 | 6.743 | 0.010 | 6.242 | 0.010 |
| NTU4DRadLM baseline: Fast-LIO [25] | 4.178 | 0.083 | 4.759 | 0.030 | 8.221 | 0.010 | 7.120 | 0.011 |
| Our method (GICP scan matching) | 1.746 | 0.035 | 4.142 | 0.020 | 3.902 | 0.005 | <u>3.781</u> | 0.006 |
| Our method (single hypothesis) | <u>1.501</u> | 0.030 | 3.133 | <u>0.015</u> | <u>2.851</u> | 0.004 | 4.529 | <u>0.007</u> |
| Our method (full version) | 1.383 | <u>0.028</u> | 2.934 | 0.014 | 3.413 | <u>0.005</u> | 4.259 | 0.006 |

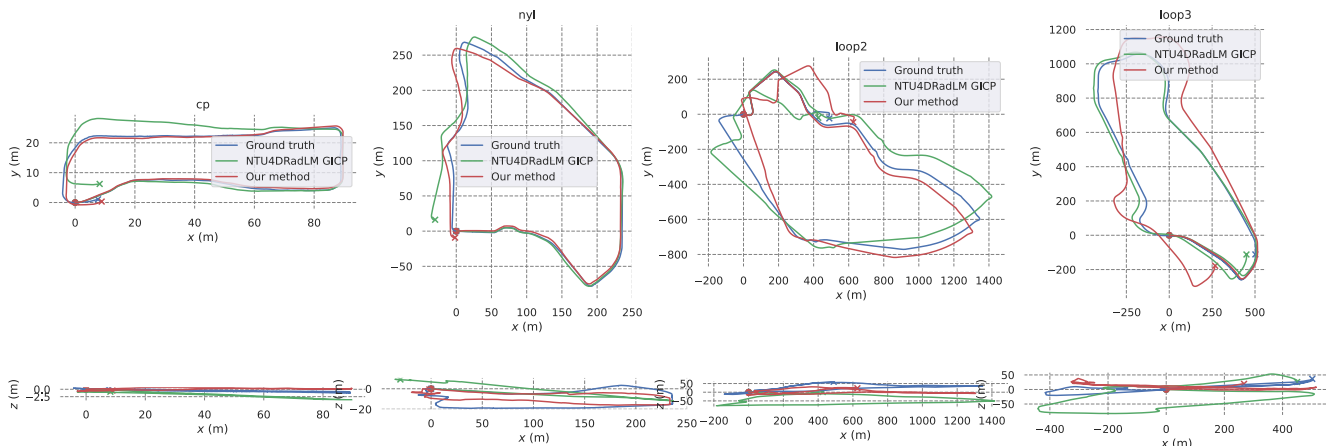


Fig. 3. Generated trajectories for the 4 tested NTU4DRadLM sequences.

B. Qualitative Analysis

Figure 3 shows the plotted trajectories of the ground truth, NTU4DRadLM GICP baseline and the full version of our method; across the 4 sequences. We can observe that in the low speed sequences (cp, nyl) our method accumulates substantially less drift in the XY plane, and manages to closely match the ground truth. High speed sequences (loop2, loop3) prove to be more challenging for both methods; in particular, our method drifts the most in loop3 with respect to the ground truth. On the other hand, our method performs much better than the baseline in the XZ plane across all 4 sequences. In particular, in loop2 and loop3 our method avoids large drifts in the

Z axis, compared to the drifts in the baseline of over 70 meters. We think the higher accuracy in the XZ plane for our methods is responsible for improved quantitative results in these sequences, despite the lower accuracy in the XY plane.

C. Summary of results

We consider that the results described above validate our methodology. Our methods produce better relative translation and rotation metrics in 3 out of 4 tested sequences. Moreover, they produce generally better results regarding Z axis drift. Our ablation experiments also validate the Gaussian-based modeling and scan matching algorithm, as well as the multi-hypothesis approach; which contribute to improve both

estimation accuracy and robustness.

VII. CONCLUSION

In this paper we introduce a multi-hypothesis Gaussian-based radar-inertial odometry pipeline. Our methods summarize noisy 4D radar scans using freely positioned 3D Gaussians (like 3DGS [8] and unlike NDT [2]), which then support multi-hypothesis scan matching for increased robustness. We show that the fusion of these methods into an EKF produces better quantitative and qualitative results than existing baselines using traditional scan matching algorithms.

Future works include improving the Gaussian modeling and scan-matching algorithms (in particular, exploring optimization algorithms more direct than gradient descent), modeling kinematic restrictions relevant to the robot platform used in order to reduce noise during egoveLOCITY estimation, further refining the pose estimates by means of Pose Graph Optimization (PGO), incorporating a loop closure module, and creating a global Gaussian map of the environment for the purposes of full SLAM.

ACKNOWLEDGMENT

This work was partially supported by the following grants: 1) INSERTION PID2021-127648OB-C31, and 2) NORDIC TED2021-132476B-I00 projects, funded by MCIN/AEI/10.13039/501100011033 and the “European Union NextGenerationEU / PRTR”.

REFERENCES

- [1] Anonymous, “Gaussian-SLAM: Photo-realistic Dense SLAM with Gaussian Splatting,” *Submitted to Transactions on Machine Learning Research*, 2024, under review. [Online]. Available: <https://openreview.net/forum?id=sbkKi8snqH>
- [2] P. Biber and W. Strasser, “The normal distributions transform: a new approach to laser scan matching,” in *Proceedings 2003 IEEE/RSJ International Conference on Intelligent Robots and Systems (IROS 2003) (Cat. No.03CH37453)*, vol. 3, 2003, pp. 2743–2748 vol.3.
- [3] C. Doer and G. F. Trommer, “An EKF Based Approach to Radar Inertial Odometry,” in *2020 IEEE International Conference on Multi-sensor Fusion and Integration for Intelligent Systems (MFI)*, 2020, pp. 152–159.
- [4] —, “Radar Inertial Odometry with Online Calibration,” in *2020 European Navigation Conference (ENC)*, 2020, pp. 1–10.
- [5] P.-E. Forssén, “Low and Medium Level Vision using Channel Representations,” Ph.D. dissertation, Linköping University, Sweden, SE-581 83 Linköping, Sweden, March 2004, appendix C, Dissertation No. 858, ISBN 91-7373-876-X.
- [6] M. Grupp, “evo: Python package for the evaluation of odometry and SLAM.” <https://github.com/MichaelGrupp/evo>, 2017.
- [7] N. Keetha, J. Karhade, K. M. Jatavallabhula, G. Yang, S. Scherer, D. Ramanan, and J. Luiten, “SplaTAM: Splat Track & Map 3D Gaussians for Dense RGB-D SLAM,” in *Proceedings of the IEEE/CVF Conference on Computer Vision and Pattern Recognition (CVPR)*, June 2024, pp. 21 357–21 366.
- [8] B. Kerbl, G. Kopanas, T. Leimkühler, and G. Drettakis, “3D Gaussian Splatting for Real-Time Radiance Field Rendering,” *ACM Transactions on Graphics*, vol. 42, no. 4, July 2023. [Online]. Available: <https://repo-sam.inria.fr/fungraph/3d-gaussian-splatting/>
- [9] K. Koide, “small_gicp: Efficient and parallel algorithms for point cloud registration,” *Journal of Open Source Software*, vol. 9, no. 100, p. 6948, Aug. 2024.
- [10] P.-C. Kung, C.-C. Wang, and W.-C. Lin, “A Normal Distribution Transform-Based Radar Odometry Designed For Scanning and Automotive Radars,” in *2021 IEEE International Conference on Robotics and Automation (ICRA)*, 2021, pp. 14 417–14 423.
- [11] M. Magnusson, “The Three-Dimensional Normal-Distributions Transform — an Efficient Representation for Registration, Surface Analysis, and Loop Detection,” Ph.D. dissertation, Örebro University, December 2009.
- [12] H. Matsuki, R. Murai, P. H. Kelly, and A. J. Davison, “Gaussian Splatting SLAM,” in *Proceedings of the IEEE/CVF Conference on Computer Vision and Pattern Recognition (CVPR)*, June 2024, pp. 18 039–18 048.
- [13] B. Mildenhall, P. P. Srinivasan, M. Tancik, J. T. Barron, R. Ramamoorthi, and R. Ng, “NeRF: Representing Scenes as Neural Radiance Fields for View Synthesis,” in *ECCV*, 2020.
- [14] J. Ortiz, A. Clegg, J. Dong, E. Sucar, D. Novotny, M. Zollhoefer, and M. Mukadam, “iSDF: Real-Time Neural Signed Distance Fields for Robot Perception,” in *Robotics: Science and Systems*, 2022.
- [15] P. Pfreundschuh, H. Oleynikova, C. Cadena, R. Siegwart, and O. Andersson, “COIN-LIO: Complementary Intensity-Augmented LiDAR Inertial Odometry,” in *2024 IEEE International Conference on Robotics and Automation (ICRA)*. IEEE, 2024, pp. 1730–1737.
- [16] J. Rehder, J. Nikolic, T. Schneider, T. Hinzmann, and R. Siegwart, “Extending kalibr: Calibrating the extrinsics of multiple IMUs and of individual axes,” in *2016 IEEE International Conference on Robotics and Automation (ICRA)*, 2016, pp. 4304–4311.
- [17] A. Segal, D. Hähnel, and S. Thrun, “Generalized-ICP,” in *Robotics: Science and Systems*. The MIT Press, 2009.
- [18] J. Solà, “Quaternion kinematics for the error-state Kalman filter,” 2017. [Online]. Available: <https://arxiv.org/abs/1711.02508>
- [19] V. Spruyt, “A geometric interpretation of the covariance matrix,” May 2021, accessed: December 2024. [Online]. Available: <https://www.visiondummy.com/2014/04/geometric-interpretation-covariance-matrix/>
- [20] D. Wang, S. May, and A. Nuechter, “RIV-SLAM: Radar-Inertial-Velocity optimization based graph SLAM,” in *2024 IEEE 20th International Conference on Automation Science and Engineering (CASE)*, 2024, pp. 774–781.
- [21] H. Wang, C. Wang, C. Chen, and L. Xie, “F-LOAM: Fast LiDAR Odometry and Mapping,” in *2021 IEEE/RSJ International Conference on Intelligent Robots and Systems (IROS)*, 2020.
- [22] X. Wu, Y. Chen, Z. Li, Z. Hong, and L. Hu, “EFEAR-4D: Ego-Velocity Filtering for Efficient and Accurate 4D radar Odometry,” 2024. [Online]. Available: <https://arxiv.org/abs/2405.09780>
- [23] J. Zhang and S. Singh, “LOAM: Lidar Odometry and Mapping in Real-time,” in *Robotics: Science and Systems*, 07 2014.
- [24] J. Zhang, R. Xiao, H. Li, Y. Liu, X. Suo, C. Hong, Z. Lin, and D. Wang, “4DRT-SLAM: Robust SLAM in Smoke Environments using 4D Radar and Thermal Camera based on Dense Deep Learnt Features,” in *2023 IEEE International Conference on Cybernetics and Intelligent Systems (CIS) and IEEE Conference on Robotics, Automation and Mechatronics (RAM)*, 2023, pp. 19–24.
- [25] J. Zhang, H. Zhuge, Y. Liu, G. Peng, Z. Wu, H. Zhang, Q. Lyu, H. Li, C. Zhao, D. Kircali, S. Mharolkar, X. Yang, S. Yi, Y. Wang, and D. Wang, “NTU4DRadLM: 4D Radar-Centric Multi-Modal Dataset for Localization and Mapping,” in *2023 IEEE 26th International Conference on Intelligent Transportation Systems (ITSC)*, 2023, pp. 4291–4296.
- [26] J. Zhang, H. Zhuge, Z. Wu, G. Peng, M. Wen, Y. Liu, and D. Wang, “4DRadarSLAM: A 4D Imaging Radar SLAM System for Large-scale Environments based on Pose Graph Optimization,” in *2023 IEEE International Conference on Robotics and Automation (ICRA)*, 2023, pp. 8333–8340.
- [27] Z. Zhang and D. Scaramuzza, “A Tutorial on Quantitative Trajectory Evaluation for Visual-(Inertial) Odometry,” in *IEEE/RSJ Int. Conf. Intell. Robot. Syst. (IROS)*, 2018.